




The case study of a brittle failure of a mountain bike frame composed by carbon fiber reinforced plastic

Rani F. El Hajjar¹  | Alessandro Pegoretti²  | Alexander Movchan³ |
Paolino De Falco⁴ | Nicola M. Pugno^{4,5} 

¹Engineering Mechanics and Composites Research Laboratory, College of Engineering, University of Wisconsin-Milwaukee, Milwaukee, Wisconsin, USA

²Department of Industrial Engineering, University of Trento, Trento, Italy

³Department of Mathematical Science, University of Liverpool, Liverpool, UK

⁴School of Engineering and Material Science, Queen Mary University of London, London, UK

⁵Laboratory for Bioinspired, Bionic, Nano, Meta, Materials and Mechanics, Department of Civil, Environmental and Mechanical Engineering, University of Trento, Trento, Italy

Correspondence

Nicola M. Pugno, Laboratory for Bioinspired, Bionic, Nano, Meta, Materials and Mechanics, Department of Civil, Environmental and Mechanical Engineering, University of Trento, Trento, Italy.
Email: nicola.pugno@unitn.it

Abstract

A mountain bike carbon reinforced polymeric frame failed in two pieces during cycling over a grass meadow at a speed of about 25 km/h. This has caused the shoulder dislocation of the driver, also last author of this paper. Here, we demonstrate evidence of macroscopic numerous pre-existing and propagating defects, such as wrinkles, voids and delaminations, resulting in low mechanical properties of this frame. Numerical dynamic simulations conclude the paper and suggest a further cause of frame weakening, due to defect-resonance interaction. The paper suggests that the design of carbon fiber reinforced plastic frame for mountain bikes may require new scientific and technological advancements for the safety of the riders, at least today carefully eliminating pre-existing defects and tomorrow proposing bioinspired flaw tolerant solutions.

KEYWORDS

bike frame, brittle fracture, carbon fibers, polymer composites

1 | INTRODUCTION

On September 4th 2015 (whilst trying to avoid a rally car) the last author went off a paved road and onto a grass meadow at a speed of around 25 km/h. After a few meters and small bumps in the ground the bike broke in two. The driver fell off the bike after it broke—not before—and dislocated his shoulder.

In this paper, we demonstrate the evidence of macroscopic numerous pre-existing and propagating defects, such as wrinkles, voids and delaminations, resulting in low mechanical properties of this frame.

Given the morphology of wrinkles observed, the static strength and stiffness in the areas around the wrinkling zone are expected to be more than 50% lower than pristine or unwrinkled portions away from this region and the fatigue life reduced by more than 10.^{1–36} This type of defects are by sure pre-existing.

The bicycle frame examination also showed multiple regions with several areas of wide spread delaminations and voids. The processing of tubular frame sections requires careful design to prevent the occurrence of low-pressure regions during the curing process. The presence of poor consolidation is

This is an open access article under the terms of the [Creative Commons Attribution-NonCommercial-NoDerivs](https://creativecommons.org/licenses/by-nc-nd/4.0/) License, which permits use and distribution in any medium, provided the original work is properly cited, the use is non-commercial and no modifications or adaptations are made.

© 2023 The Authors. *Polymer Composites* published by Wiley Periodicals LLC on behalf of Society of Plastics Engineers.

evidence of poor manufacturing procedures that occurred during the fabrication of this frame. The effect of consolidation on the mechanical properties has been documented extensively in the literature^{17,37-47} and could also dramatically affect the final mechanical resistance. This type of defects can be pre-existing or propagating.

Accordingly pre-existing fiber wrinkling were responsible for the premature brittle failure of this frame, as due to a low quality production, in spite to the top level of this frame. Additional pre-existing or propagating delaminations and voids were also responsible to the observed brittle behavior.

Numerical dynamic simulations conclude the paper and suggest a further cause of frame weakening, due to defect-resonance interaction.

2 | DENSITY MEASUREMENTS, FIBER WEIGHT OR VOLUME FRACTIONS, MICROPOROSITY, AND RESIN CURING

2.1 | Density measurements

Density measurements were made by cutting small (mass between 0.2 and 0.6 g) samples from the bike frame and weighing them in air (m_{air}) and when immersed in ethylic alcohol (m_{liquid}). For ethylic alcohol a density ρ_{liquid} at room temperature of 0.8089 g/cm³ was considered. The density (ρ_{exp}) was then estimated by using the following formula:

$$\rho_{\text{exp}} = \frac{\rho_{\text{liquid}} m_{\text{air}}}{m_{\text{air}} - m_{\text{liquid}}} \quad (1)$$

The measured values are reported in Table 1 and a density of 1.4743 to +0.0263 g/cm³ emerges.

2.2 | Measurements of the fiber weight fraction by thermogravimetric analysis

The fiber weight content has been measured by thermogravimetric analysis (TGA) on a small (about 60 mg) sample cut from the bike frame. TGA measurements were performed on a TA Q5000 machine under a nitrogen flux of 100 mL/min at a heating rate of 10°C/min. The obtained thermogram is reported in Figure 1. The observed total weight loss at 700°C is of 38.62%. Therefore the fiber weight fraction can be estimated to be 61.38%.

TABLE 1 Density measurements.

Weight in air, m_{air} (g)	Weight in ethylic alcohol, m_{liquid} (g)	Density, ρ_{exp} (g/cm ³)
0.6622	0.2958	1.4619
0.6160	0.2988	1.4786
0.6404	0.2988	1.5165
0.2114	0.0949	1.4678
0.2035	0.087	1.4465
	Mean	1.4743
	Standard deviation	0.0263

2.3 | Estimation of theoretical density

The theoretical density can be evaluated according to the following formula:

$$\rho_{\text{th}} = \frac{1}{\frac{W_f}{\rho_f} + \frac{W_m}{\rho_m}}, \quad (2)$$

where, W_f and W_m are the fiber and resin weight fractions respectively. The fiber (ρ_f) and resin (ρ_m) densities were assumed to be equal to 1.76 g/cm³ (typical of AS4 carbon fibers) and 1.15 (typical resin) g/cm³, respectively. Accordingly, a theoretical density ρ_{th} of 1.4733 g/cm³ can be estimated.

Therefore, the correspondence between the theoretical and experimental density values indicates that a very small microporosity content is present in the investigated samples.

2.4 | Volume fraction of fibers

From the obtained data, the fiber weight fraction (W_f) can be also converted into a fiber volume fraction (V_f) by using the following relationship:

$$V_f = \frac{1}{1 + \frac{\rho_f}{\rho_m} \left(\frac{1}{W_f} - 1 \right)}. \quad (3)$$

In this way, a fiber volume fraction of 50.52% can be estimated.

2.5 | Differential scanning calorimetry

Differential scanning calorimetry (DSC) measurements were performed on specimens of about 20 mg extracted from the bike frame. Tests were performed with a Mettler DSC 30 apparatus under nitrogen flux of 100 mL/min at

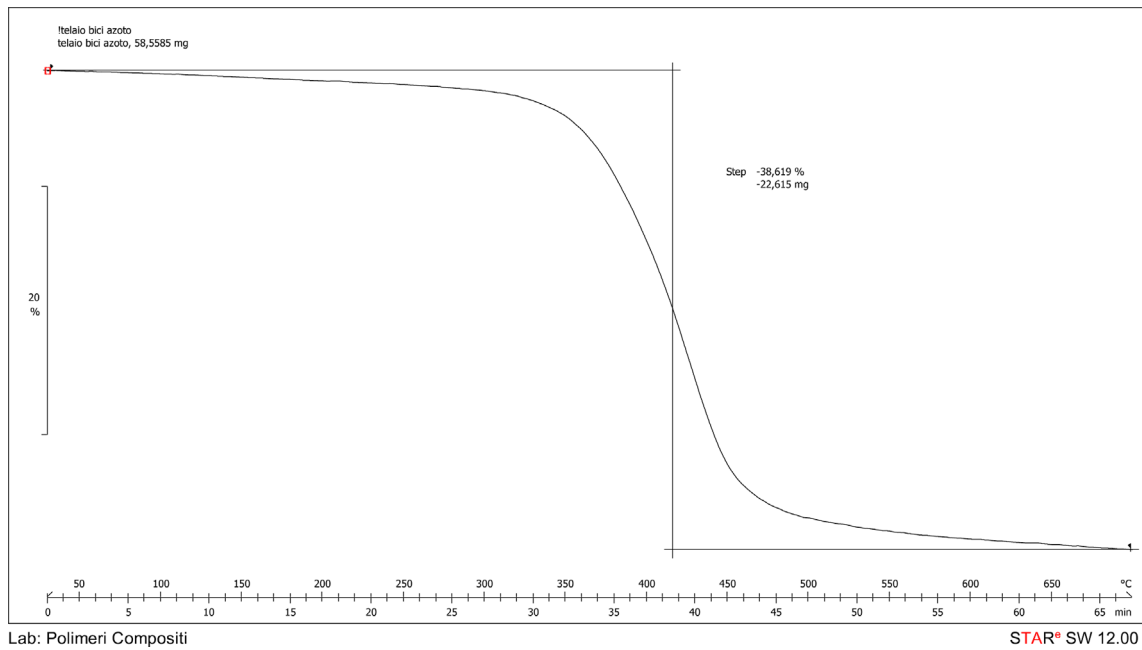


FIGURE 1 Thermogravimetric analysis thermogram under inert atmosphere.

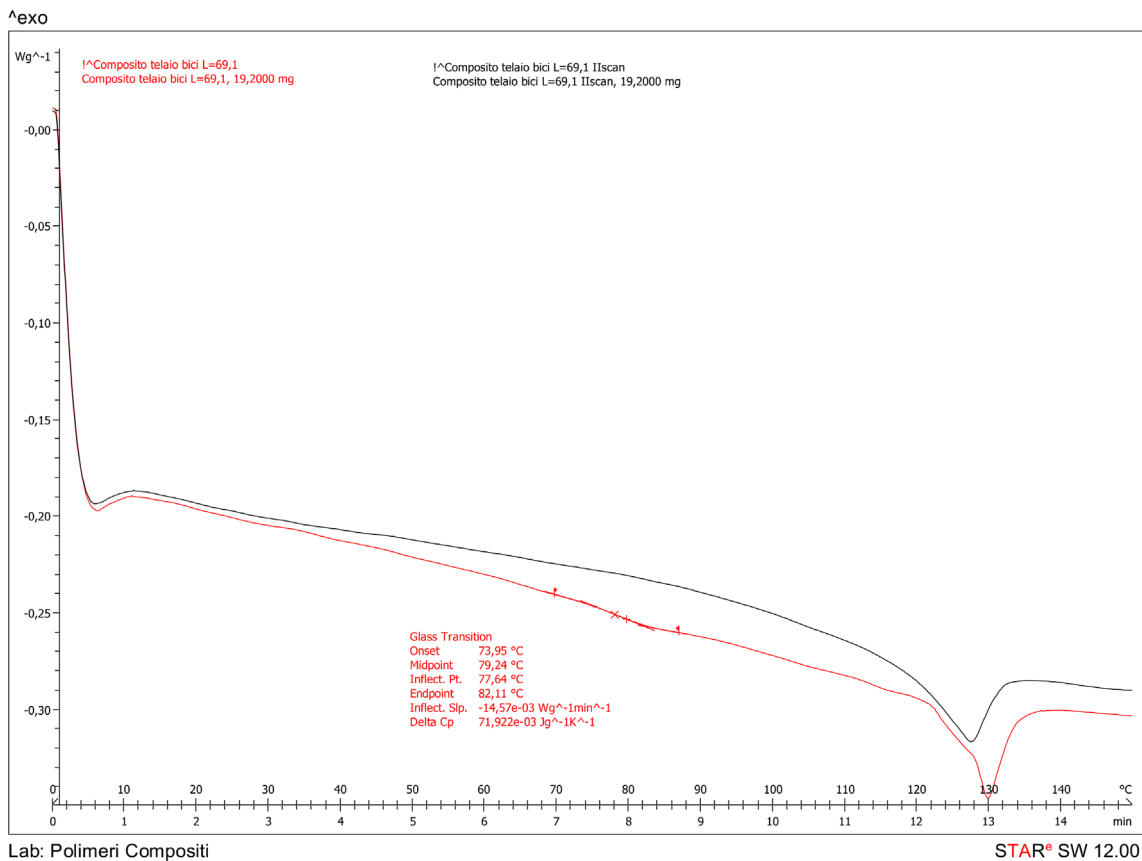


FIGURE 2 Differential scanning calorimetry thermograms of first and second heating scans.

a heating/cooling rate of 10°C/min. The obtained thermograms are reported in Figure 2 for as the first and second scan it is concerned.

From the DSC thermograms, it can be concluded that the resin in the composite material is fully cured with a glass transition temperature of about 78°C. The melting

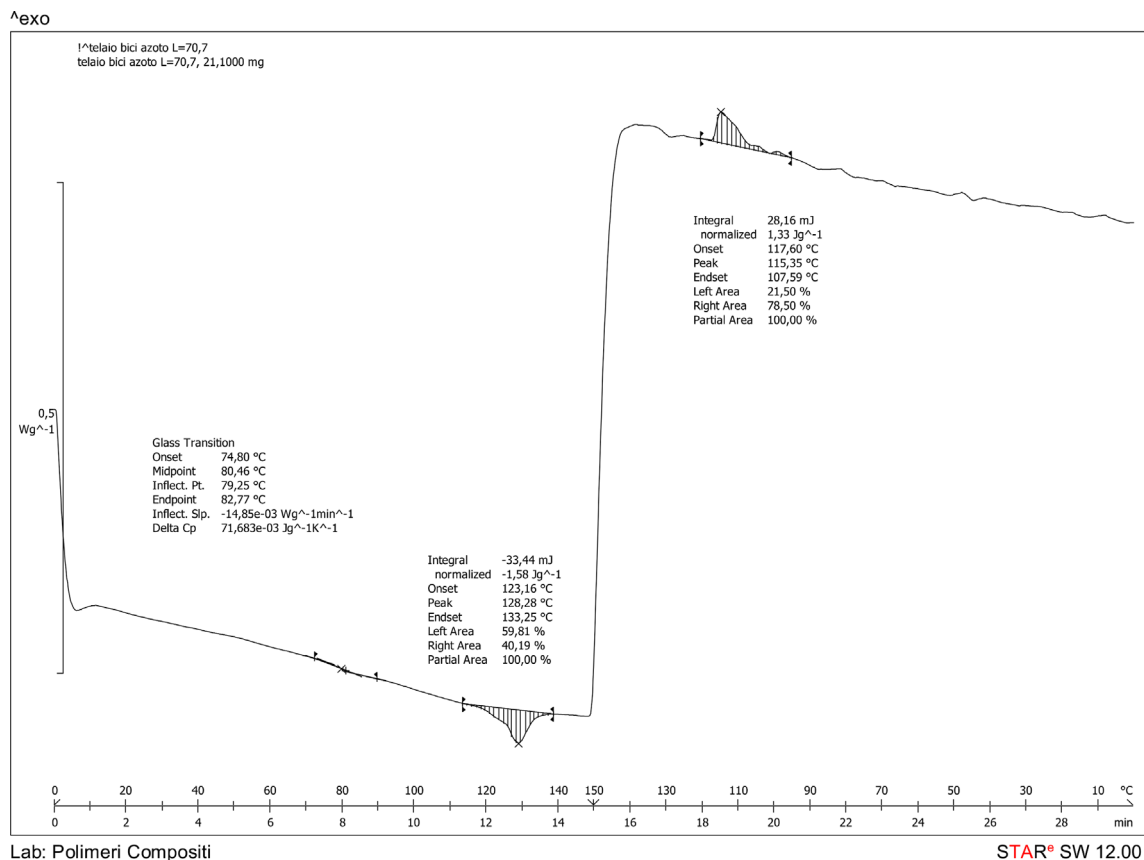


FIGURE 3 Differential scanning calorimetry thermograms of third heating cooling scans.

peak located at about 130°C can be attributed to a thermoplastic material (probably polyethylene). In fact, even by naked eyes inspection, some white fibers can be noticed. This additional phase will be discussed in the next sections. A third DSC scan followed by a cooling scan confirmed that the signal is related to a crystallization process of a thermoplastic polymer, Figure 3.

3 | INVESTIGATIONS OF MICRO-, MESO- AND MACRO-STRUCTURAL DEFECTS

In this part of the study, we investigate the micro-, meso- and macro-structural defects that are typically associated with reducing the mechanical performance of carbon-fiber reinforced polymer composites. It is important to distinguish between cosmetic defects (e.g., scratches in the paint or benign resin pockets) and primary defects degrading the mechanical performance. The primary defects in composites that are known to compromise the structural integrity are voids, delaminations and fibers wrinkling. Thus any processing method has to be effectively designed to eliminate or minimize these defects.

The bladder or internal pressure approach used in producing the composite in the bicycle frame, if not done correctly, can lead to air entrapment due to the tight radii, high ply angles and relatively thick sections. The high restraints can result in low-pressure regions even when high internal pressures are applied during curing. In addition, careless manufacturing procedures and lack of quality control during the trim, collation and curing process can also lead to detrimental fiber distortions or wrinkles, which also disrupt the load carrying capacity and result in significant degradations in mechanical properties.

In undertaking the investigation of the frame, the microstructure of the composite laminate is examined using optical microscopy methods. A large portion of one of the two pieces of the frame, including the top and down tube around the fracture regions, was sectioned into several samples. The sample numbers were 2, 3, 4, 5, 6, 7, 10, 11, 12, 13, 14, and 15. The samples numbered 8, 16, and 17 are parts that were the nearest to the fracture location. The samples are numbered from the front of the bicycle with sample numbers from 1 (not investigated here) to 17. On the frame, “UP” is inserted to show which way was up on the bicycle, “F” to show which end faced the Front of the frame and “B” for which end faced

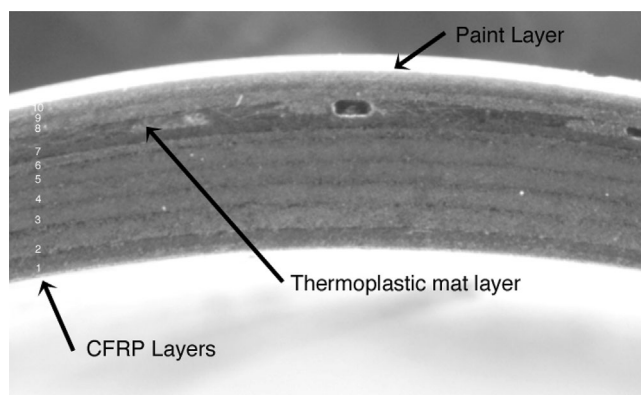


FIGURE 4 Cross section of composite showing well typical cross-section profile in top tube.

the back of the frame respectively. Care was taken during the sectioning process to preclude any damage to the laminate by using specialized thin diamond blades followed with polishing using 320, 600, 800, and 1200 grit sandpapers. Figure 4 reports the micrograph of a cross-section from the bike showing the paint layer and the carbon fiber reinforced plastic (CFRP) plys. Note the presence of an additional layer of a thermoplastic fiber mat in the laminate stack as already mentioned and to be discussed in the next sections.

3.1 | Ply cutting and collation issues: evidence of macroscopic multiple wrinkle defects

Numerous instances of severe wrinkling are discovered from the micrographic inspections. Figure 5 shows a large wrinkle in two of the sections from the top tube. The presence of large amounts of out-of-plane wrinkling (or fiber waviness) point to poor handling of the plys during the ply cutting and collation process. The oversized plys appear to have been mishandling during the collation process in the tool leading to the wrinkle defects. The wrinkle defects found in multiple locations on the bike frame fall under the category of severe wrinkling defects not acceptable for high performance composite applications where good dynamic, fatigue and static strength performances are desired.

The acceptable industry practices on fiber waviness typically tolerate low amounts of fiber wrinkling based on the waviness aspect ratio. A wrinkle aspect ratio (length divided by height) greater than 15 is considered acceptable. As the aspect ratio approaches infinity the ply is considered perfectly straight while an aspect ratio below 15 indicates severe impact on the composite design. The wrinkle in Figure 5A does not only have an aspect ratio of

approximately 8 but is also coupled with the load path being completely disrupted by the folding over for 2 plys. A similar defect from another section is also shown for comparison in Figure 5B. It is important to note that the wrinkle from 6B appears to have run all the way across the tube to the front of the frame when observed at 6F. Large wrinkles are also observed in the cross-sectional scans in samples 2, 3, 4, 5, and 6. In many cases the same wrinkle extends through the multiple sections examined. Given the morphology of wrinkles observed, the static strength and stiffness in the areas around the wrinkling zone are expected to be more than 50% lower than pristine or unwrinkled portions away from this region and the fatigue life reduced by more than 10.^{1–36}

3.2 | Curing and consolidation issues: evidence of macroscopic multiple delamination defects

As stated, the bicycle frame examination also showed multiple regions with several areas of wide spread delaminations. The processing of tubular frame sections requires careful design to prevent the occurrence of low-pressure regions during the curing process. The presence of poor consolidation is evidence of poor manufacturing procedures that occurred during the fabrication of this frame. The effect of consolidation on the mechanical properties has been documented extensively in the literature.^{17,37–47}

Every section of the frame examined contained multiple interfaces that are affected (Figure 6A). In one section near the fracture zone a large void is observed at the tube radii (Figure 6B). Curved parts are sensitive to the tooling, stacking sequence, part thickness and resin properties. Resin migration, disbonds, fiber waviness and porosity can all occur in the curved regions when improper processing takes place.⁴⁸ Other defects observed in the examined frame that are also associated with poor consolidation at the tube radii include blisters in the inner tube and non-uniform ply thicknesses or resin thinning.

Such macroscopic delaminations are even more critical than the previously observed wrinkles. The defects are so numerous, large and close that their interaction and further weakening is expected.

3.3 | An additional material not well integrated: evidence of macroscopic multiple void defects

During the investigation of the fractured parts, as already mentioned, we have observed the presence of what

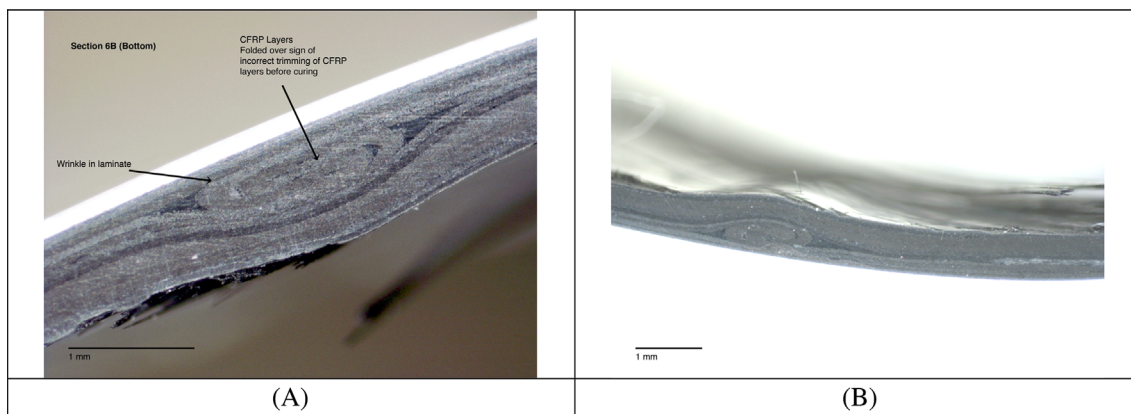


FIGURE 5 (A) Large wrinkle due to the carbon fiber reinforced plastic (CFRP) ply folding over during the ply collation process (Section 6B). (B) Large wrinkle in top tube in Sample 7F.

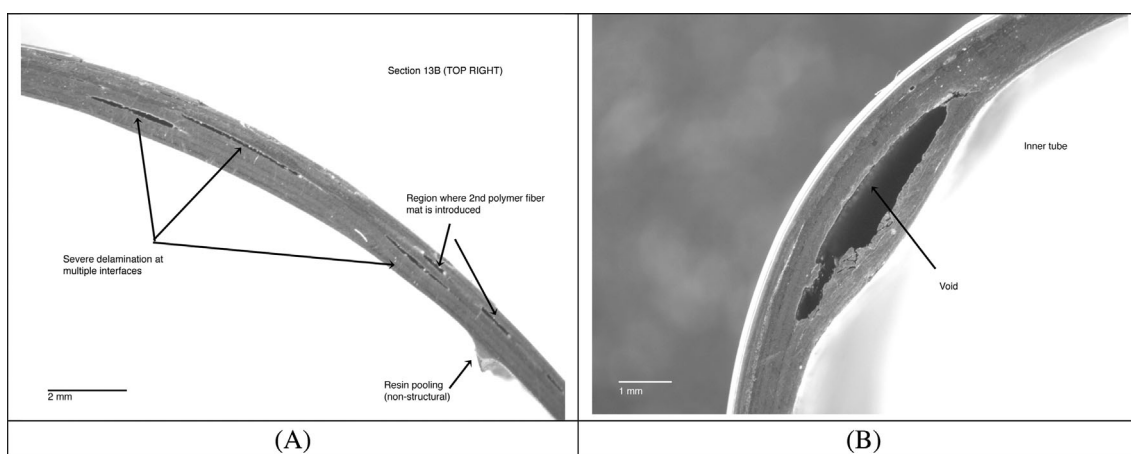


FIGURE 6 (A) Multiple delamination sites at various interfaces in Section 13B. (B) Large void due to improper consolidation in Section 7F.

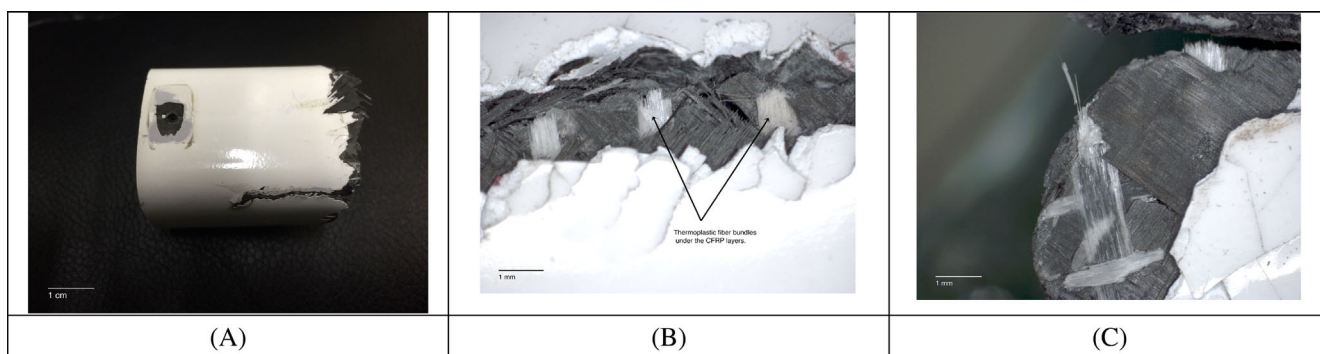


FIGURE 7 (A) Top tube fracture region (note this is the section adjacent to Sample 8 face b). See part (B) for close-up of fracture region. (B) Close-up of fracture zone in top tube showing thermoplastic fibers in failure region; note the thermoplastic fiber bundles are located within the carbon fiber reinforced plastic (CFRP) stack. (C) Close-up of region containing thermoplastic fiber mat.

appeared to be white colored filaments in the fracture zone (Figure 7A–C). The microstructural investigation confirms the presence of a 2nd material system directly present and impacting the structural performance of the

composite material beyond the carbon fiber and the polymeric resin. The filaments appear to be polymer fiber bundles and are in the form of a fiber mat that is present along the sides of the tubes (both top and down tubes).

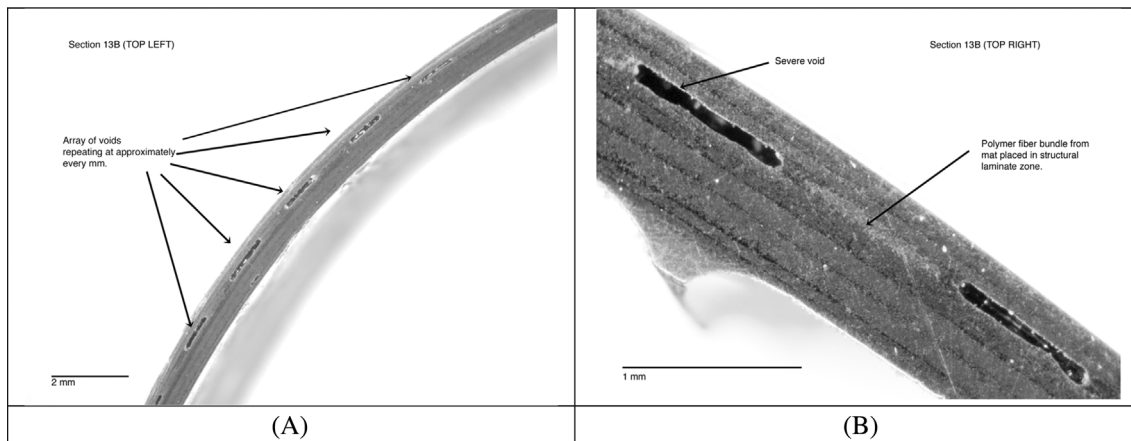


FIGURE 8 (A) Large voids corresponding to the gaps in the polymer fiber mat. (B) Close-up showing large voids occurring after several layers from the outer surface in the region corresponding to the thermoplastic fiber mat.

TABLE 2 Tensile and bending moduli and notch and shear strengths as obtained from our experiments. Hole size is 0.476 cm and width is 1.778 cm.

Section	Estimated number of plies	Thickness (mm)	Tension modulus (GPa)	Bending modulus (GPa)	Delamination stress (MPa)	Max notched tension failure stress (MPa)
2	9.000	1.524	36.75	14.55	0.221	25.25
4	7.583	1.308	39.71	26.82	0.348	
6	5.306	0.961	37.09	16.62	0.185	30.00
10b	15.278	2.481	33.99	21.93	0.126	
10t	7.639	1.317	48.95	50.75	0.341	25.31
12b	6.639	1.164	55.23	27.92	0.419	
12t	5.611	1.008	43.92	14.41	0.208	40.21
14b	5.056	0.923	38.33	32.13	0.358	
14s	4.944	0.906	41.23	42.61	0.391	25.25

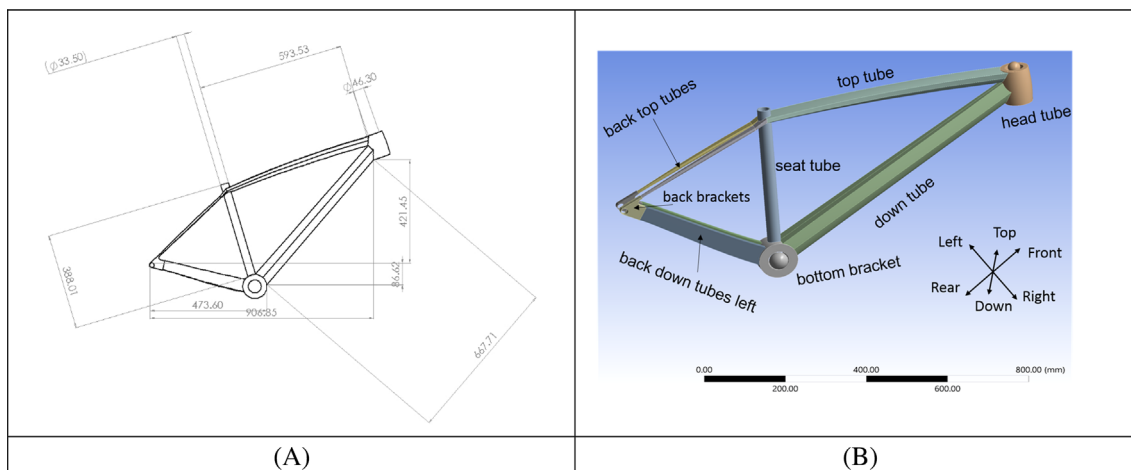


FIGURE 9 (A) Geometries (sizes in mm) considered in the numerical simulations. (B) Adopted nomenclature.

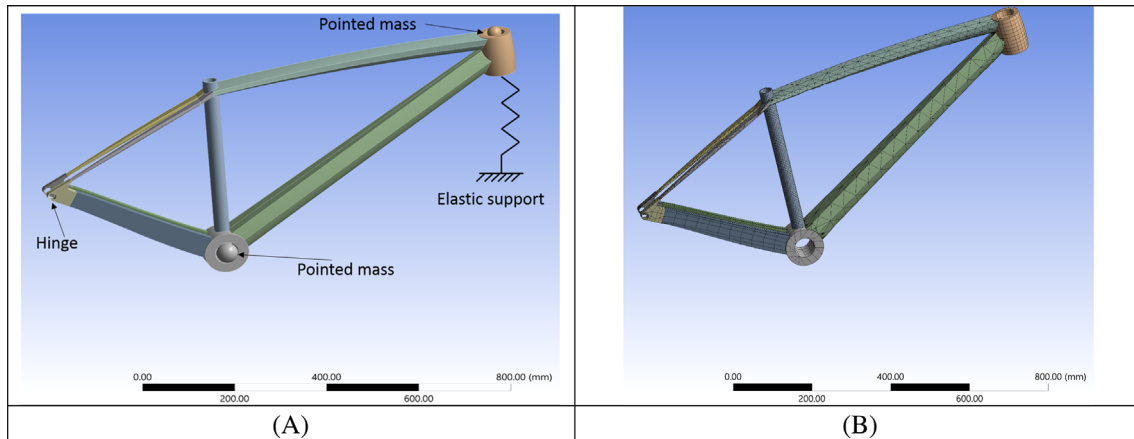
TABLE 3 Geometrical properties of the single parts.

Object name	Bottom bracket	Seat tube	Down tube	Head tube	Top tube	Back top tube left	Back top tube right	Back bracket right	Back bracket left	Back down tube right	Back down tube left
Bounding box											
Length X	97.9 mm	142.32 mm	481.31 mm	99.151 mm	580.22 mm	271.71 mm	62.316 mm	336.3 mm			
Length Y	97.9 mm	381.54 mm	565.87 mm	117.52 mm	228.49 mm	267.64 mm	66.389 mm	125.92 mm			
Length Z	68 mm	33.5 mm	64.016 mm	75.708 mm	56.8 mm	28.639 mm	16 mm	16.575 mm			
Properties											
Volume	3.6523e+005 mm ³	1.117e+005 mm ³	1.2175e+005 mm ³	3.1499e+005 mm ³	1.1342e+005 mm ³	54,605 mm ³	30,680 mm ³	51,100 mm ³			
Mass	0.61723 kg	0.18878 kg	0.20576 kg	0.53233 kg	0.19167 kg	9.2282e-002 kg	5.1849e-002 kg	8.6359e-002 kg			
Centroid X	2.1195e-003 mm	-68.362 mm	242.03 mm	499.17 mm	183.5 mm	-231.81 mm	-392.25 mm	-201.79 mm			-201.78 mm
Centroid Y	-3.8087e-015 mm	230.79 mm	286.98 mm	572.51 mm	502.89 mm	276.78 mm	93.864 mm	42.476 mm			42.472 mm
Centroid Z	-9.5882e-016 mm	2.8623e-006 mm	-0.75287 mm	-6.8829e-007 mm	5.3289e-002 mm	-17.289 mm	19,008 mm	19,256 mm	-19,008 mm	19,256 mm	-19,256 mm
Moment of inertia Ip1	709.28 kg mm ²	2350.5 kg mm ²	7873.2 kg mm ²	601.26 kg mm ²	86.246 kg mm ²	3.45 kg mm ²	3.4453 kg mm ²	24.726 kg mm ²	24.726 kg mm ²	24.724 kg mm ²	24.724 kg mm ²
Moment of inertia Ip2	709.25 kg mm ²	43.618 kg mm ²	173 kg mm ²	456.18 kg mm ²	5875.6 kg mm ²	919.7 kg mm ²	918.54 kg mm ²	805.36 kg mm ²	805.36 kg mm ²	805.22 kg mm ²	805.22 kg mm ²
Moment of inertia Ip3	944.13 kg mm ²	2350.5 kg mm ²	7867 kg mm ²	601.27 kg mm ²	5838.7 kg mm ²	917.27 kg mm ²	916.12 kg mm ²	823.18 kg mm ²	823.18 kg mm ²	823.04 kg mm ²	823.04 kg mm ²
Statistics											
Nodes	468	14,355	2827	1394	2906	873	1314	618	1163	1455	1456
Elements	72	2225	1273	220	1382	368	623	84	532	275	308

TABLE 4 Thickness of single parts' walls.

Thickness (mm)	Down tube			
Front section	Top: 1.31	Right: 1.1	Down: 1.41	Left: 1.2
Rear section	Top: 1.23	Right: 1.56	Down: 1.2	Left: 1.5
Thickness (mm)	Top tube			
Front section	Top: 1.15	Right: 0.97	Down: 0.75	Left: 1.15
Rear section	Top: 1.12	Right: 1.05	Down: 1	Left: 0.91

Note: Values were measured on the real frame (see Figure 9 for the definition of the orientation vectors).

**FIGURE 10** (A) Applied boundary conditions. (B) Adopted mesh.**TABLE 5** Properties of the pointed masses.

Object name	Point mass	Point mass 2
State	Fully defined	
Scope		
Coordinate system	Global coordinate system	
X Coordinate	2.1196e-003 mm	482.71 mm
Y Coordinate	4.2448e-017 mm	619.72 mm
Z Coordinate	34 mm	-1.6596e-015 mm
Location	Defined	
Definition		
Mass	40 kg	30 kg

TABLE 6 Properties of the entire frame in terms of volume and mass included pointed masses.

Properties	
Volume	1.2999e+006 mm ³
Mass	72.197 kg

The mat appears to be wrapped around the high curvature regions but not completely around. In the areas examined, the polymer fiber mat is located after 2–3 layers of carbon-fiber unidirectional tape from the outer

TABLE 7 Material properties.

Density	1.69e-006 kg mm ⁻³
Young's modulus	41.69 GPa
Poisson's ratio	0.3

TABLE 8 Adopted boundary conditions.

Object name	Elastic support	Hinge
State	Fully defined	
Scope		
Scoping method	Geometry selection	
Geometry	1 Face	4 Faces
Definition		
Type	Elastic support	Displacement
Suppressed	No	
Foundation stiffness	4.5e-002 N/mm ³	
Define by	Components	
Coordinate system	Global coordinate system	
X component	0. mm	
Y component	0. mm	
Z component	0. mm	

TABLE 9 Adopted mesh.

Defaults	
Physics preference	Mechanical
Relevance	0
Shape checking	Standard mechanical
Element midside nodes	Program controlled
Sizing	
Size function	Adaptive
Relevance center	Coarse
Element size	Default
Initial size seed	Active assembly
Smoothing	Medium
Transition	Fast
Span angle center	Coarse
Automatic mesh based defeaturing	On
Defeaturing tolerance	Default
Minimum edge length	4.9707e-002 mm
Statistics	
Nodes	28,829
Elements	7362
Mesh metric	None

TABLE 10 Computed natural frequencies.

Mode	Frequency (Hz)
1.	3.3814
2.	8.8191
3.	9.1595
4.	68.298
5.	86.43
6.	111.03

surface. These results are also corroborated by DSC results previously presented and showing evidence of a thermoplastic fiber system within the laminate.

The thermoplastic fiber mat is problematic for several reasons. The mat is located a few CFRP plies from the outer surface of the composite. Thus the mat is sandwiched between structural layers and thus cannot be considered a non-structural part such as the paint or primer layer. In addition, the mat used has large gaps (greater than 1 mm), which coupled with improper compaction during cure (e.g., low pressure areas) results in large voids forming within these regions (as seen in Figure 8A,B). Note the ordered location of voids in this layer corresponding to the gaps in the mat layer. The defects are so numerous and close to each other that their interaction is expected to further weaken this frame.

In the top tube, it is observed that this thermoplastic fiber mat extends from the lower radius to the top radius regions, with the top and bottom surfaces not appearing to contain this mat layer. It is possible that this thermoplastic mat layer may have been added to reinforce this section or improve the processing although without having additional design details this remains only a speculation. It is curious that the tension failure observed in the top tube as a crack running along the top tube main axis (on both sides of the tube) occurs in this region. The curved radius region is a highly stressed region in composite tubular parts. The fracture surface does not show carbon fibers present in the laminate that are perpendicular to the crack. It is not realistic to assume that the thermoplastic mat added around the curves is enough to reinforce this area significantly due to their low volume fraction (due to large spacing). This is also coupled with the fact that the mat seriously compromises the strength and stiffness of the composite laminate in this area by allowing for severe void nucleation sites.

3.4 | Tensile and bending moduli and delamination and notch strengths

We have conducted tensile and bending tests for extracting tensile and bending moduli and also delamination and notched tensile strengths. The results are reported in Table 2. The delamination and notch strengths are expected to be very low and are observed even much lower than expected, especially for delamination. Such numbers have to be considered with caution being extremely sensitive to the presence of the defects. The tensile and bending moduli are more plausible but still lower by a factor of at least two than what expected for a proper frame. Such direct observations are thus in agreement with the previous considerations.

4 | DYNAMIC NUMERICAL SIMULATIONS: EVIDENCE OF POSSIBLE RESONANCE

We have conducted dynamical numerical simulations for checking for possible resonance problems. Due to the presence on the grass of bumps of a characteristic size of the order of 10 cm, we expect a forcing frequency imposed by the cycling velocity of 25 km/h around $25 \text{ km/h}/10 \text{ cm} = 69 \text{ Hz}$.

The data for the geometry are extrapolated from the website of a company. Here we are not interested in modeling the exact frame under consideration but rather to check for possible resonance problems. Sizes in mm

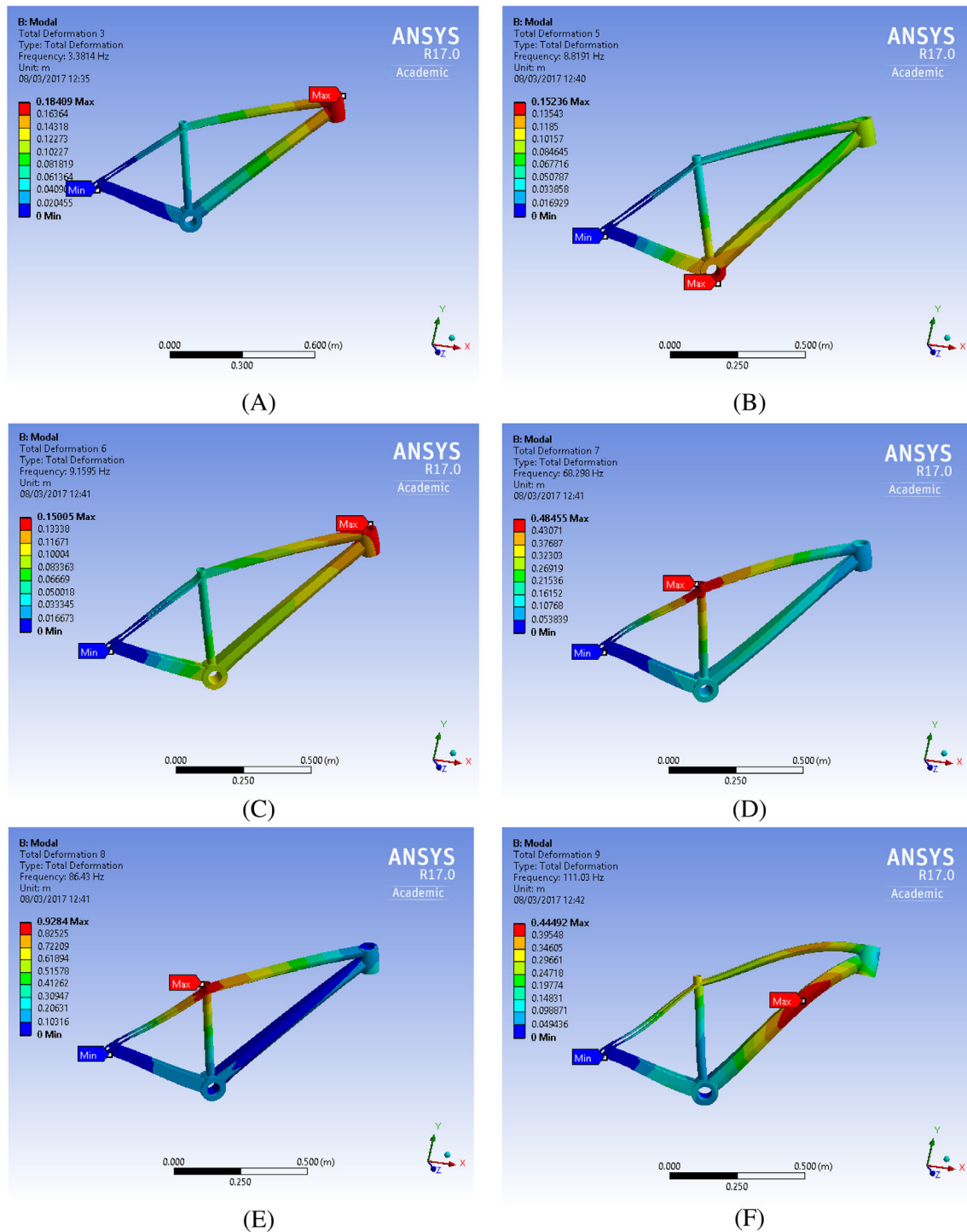


FIGURE 11 (A) Mode 1. (B) Mode 2. (C) Mode 3. (D) Mode 4. (E) Mode 5. (F) Mode 6.

are reported in Figure 9A. For the nomenclature please refer to Figure 9B. Table 3 reports the properties of the single parts. Table 4 reports the measured and thus adopted thicknesses. Figure 10A reports the applied boundary conditions. Table 5 reports the properties of the pointed masses, simulating the driver mainly placed on pedals according to the real case. Table 6 reports the volume and mass of the simulated system. Table 7 reports

the used material properties. The elastic support represents the stiffness K of the fork and its value was assumed imposing a displacement of 1 cm under a mass of 100 kg (specifically, the value of the foundation stiffness K_f (stiffness per unit area distributed on the fork cross-section) was calculated by applying the equation for a linear spring $F = -Kx$, where $F = 9.81 \text{ m/s}^2 \times 100 \text{ kg}$, $x = 1 \text{ cm}$ and knowing that the area of the section of the

fork is $A = 2.18 \times 10^{-3} \text{ m}^2$ thus as $K_f = K/A$ (Table 8). Figure 10B and Table 9 report the adopted mesh. The computed natural frequencies are reported in Table 10 and, due to the driver position/man mass real distribution and measured low elastic modulus, are observed quite low, from 3 up to 111 Hz for the first 6 modes, Figure 11A–F. Note that mode 4 has a frequency around 68 Hz and is thus compatible with a resonance imposed by the wavy nature of the grass and cycling velocity (previously computed as 69 Hz); also note that the related mode shape (Figure 11D) has the maximal relative displacement in the region of the observed fracture. We cannot thus exclude that the observed severe defects were further weakened by interaction with a dynamic resonance.

5 | CONCLUSIONS

In summary, it appears that the process used in the manufacturing of this bicycle frame was compromised by poor ply cutting, collation and processing procedures. The poor processing conditions led to the proliferation of large amounts of voids, delaminations and fibers wrinkling of the load bearing plys, as directly observed. The improper trim and collation led to the widespread wrinkles observed in the frame whereas improper consolidation during cure led to many low-pressure spots in the frame leading to large amounts of voids and delaminations.

The inclusion of the thermoplastic fiber mat in the absence of proper consolidation results in repeated large volume voids around the highly stressed curved regions of the top and bottom tube. The presence of the mat near the failed region and the morphology of the fracture show that large amounts of voids are to be expected near the fracture region.

Further, the presence of the thermoplastic material within the cross-section of the material poses an interesting question as to whether the manufacturer failed to disclose the presence of these polymer fibers. In any case, the presence of the thermoplastic fiber mat layer within the composite laminate directly leads to large voids and delaminations in many of the CFRP sections and thus cannot be considered a cosmetic or protection layer.

The very poor quality of the bicycle frame with the widespread defects shown is also expected to lead to sporadic and widespread low stiffness regions. The result of these stiffness degradations could result in the stiffer portion of the bicycle near the joints needing to carry more loads. Mechanics of materials basic principles inform us that when low and high stiffness materials are coupled (in parallel), we should expect the load redistribution to result in more loads transferred into the stiffer components and high stress concentrations will be occurring

near the joint regions and thus large amounts of defects cannot be tolerated in those regions.

Direct elastic and strength measurements confirm the previous findings.

Dynamic resonance is also demonstrated to be an additional potential problem for a so defective frame. In particular, we expected a forcing frequency imposed by the cycling velocity and bumpy substrate around 69 Hz, compatible with the natural frequency of mode 4 of the frame (68 Hz), also displaying a maximal relative displacement at the location of the observed fracture. We cannot thus exclude that the observed severe defects were further weakened by interaction with a dynamic resonance.


Given the very poor quality of manufacturing, displayed in the examined sections, it is now not anymore surprising that the frame failed in the high stress regions near the joints of both the top tube and down tube with the seat tube just under subcritical conditions.

Concluding, the defects observed in the frame are much beyond those that would be considered acceptable in the practice of manufacturing high performance carbon-fiber composite products and are thus associated to a low quality product.

DATA AVAILABILITY STATEMENT

The data that support the findings of this study are available from the corresponding author upon reasonable request.

ORCID

Rani F. El Hajjar  <https://orcid.org/0000-0003-4778-5186>

Alessandro Pegoretti  <https://orcid.org/0000-0001-9641-9735>

Nicola M. Pugno  <https://orcid.org/0000-0003-2136-2396>

REFERENCES

- Adams DO, Hyer MW. Effects of layer waviness on the compression fatigue performance of thermoplastic composite laminates. *Int J Fatigue*. 1994;16(6):385-391.
- Allison BD, Evans JL. Effect of fiber waviness on the bending behavior of S-glass/epoxy composites. *Mater Des*. 2012;36:316-322.
- Anastasi RF. *Investigation of fiber waviness in a thick glass composite beam using THz NDE*. Nondestructive Characterization for Composite Materials, Aerospace Engineering, Civil Infrastructure, and Homeland Security 2008;6934. SPIE, 2008.
- Bogetti T, Gillespie J, Lamontia M. Influence of ply waviness on the stiffness and strength reduction on composite laminates. *J Thermoplast Compos Mater*. 1992;5:344-369.
- Bradley DJ, Adams DO, Gascoigne HE. Interlaminar strains and compressive strength reductions due to nested layer waviness in composite laminates. *J Reinf Plast Compos*. 1998;17(11):989-1011.
- Chakrapani SK, Dayal V, Barnard D. Detection and characterization of waviness in unidirectional GFRP using Rayleigh wave

- air coupled ultrasonic testing (RAC-UT). *Res Nondestruct Eval*. 2013;24:191-201.
7. Chakrapani SK, Dayal V, Barnard DJ, Eldal A, Krafka R. Ultrasonic Rayleigh wave inspection of waviness in wind turbine blades: Experimental and finite element method. 2011.
 8. Chun HJ, Shin JY, Daniel IM. Nonlinear behavior of thick composites with uniform fiber waviness. *AIAA J*. 2000;38(10):1949-1955.
 9. Chun HJ, Shin JY, Daniel IM. Effects of material and geometric nonlinearities on the tensile and compressive behavior of composite materials with fiber waviness. *Compos Sci Technol*. 2001;61(1):125-134.
 10. El-Hajjar RF, Lo Ricco MT. Modified average stress criterion for open hole tension strength in presence of localised wrinkling. *Plast Rubber Compos*. 2012;41(9):396-406.
 11. El-Hajjar RF, Petersen DR. Gaussian function characterization of unnotched tension behavior in a carbon/epoxy composite containing localized fiber waviness. *Compos Struct*. 2011;93(9):2400-2408.
 12. Elhajjar R, Haj-Ali R, Wei B-S. An infrared thermoelastic stress analysis investigation for detecting fiber waviness in composite structures. *Polym-Plast Technol Eng*. 2014;53(12):1251-1258.
 13. Elhajjar RF, Shams SS. Compression testing of continuous fiber reinforced polymer composites with out-of-plane fiber waviness and circular notches. *Polym Test*. 2014;35:45-55.
 14. Hsiao HM, Daniel IM. Elastic properties of composites with fiber waviness. *Compos Part A: Appl Sci Manuf*. 1996;27(10):931-941.
 15. Hsiao HM, Daniel IM. Nonlinear elastic behavior of unidirectional composites with fiber waviness under compressive loading. *J Eng Mater Technol: Trans ASME*. 1996;118(4):561-570.
 16. Hsiao HM, Daniel IM. Effect of fiber waviness on stiffness and strength reduction of unidirectional composites under compressive loading. *Compos Sci Technol*. 1996;56(5):581-593.
 17. Issam IQ, Eric ML-H, Rani FE-H. Identification of acoustic emissions from porosity and waviness defects in continuous fiber reinforced composites. *Adv Civil Eng Mater*. 2013;2(1):37-50.
 18. Joyce PJ, Kugler D, Moon TJ. A technique for characterizing process-induced fiber waviness in unidirectional composite laminates—using optical microscopy. *J Compos Mater*. 1997;31(17):1694-1727.
 19. Karami G, Garnich M. Effective moduli and failure considerations for composites with periodic fiber waviness. *Compos Struct*. 2005;67(4):461-475.
 20. Kugler D, Joyce PJ, Moon TJ. Investigation of the effect of part length on process-induced fiber-wrinkled regions in composite laminates. *J Compos Mater*. 1997;31(17):1728-1757.
 21. Kugler D, Moon TJ. Identification of the most significant processing parameters on the development of fiber waviness in thin laminates. *J Compos Mater*. 2002;36(12):1451-1479.
 22. Kugler D, Moon TJ. The effects of mandrel material and tow tension on defects and compressive strength of hoop-wound, on-line consolidated, composite rings. *Compos Part A: Appl Sci Manuf*. 2002;33(6):861-876.
 23. Mandell J, Samborsky D, Wang L. Effects of fiber waviness on composites for wind turbine blades. Proceedings of the international SAMPE symposium and exhibition. 2003.
 24. Nikishkov G, Nikishkov Y, Makeev A. Finite element mesh generation for composites with ply waviness based on X-ray computed tomography. *Adv Eng Softw*. 2013;58:35-44.
 25. Pain D, Drinkwater BW. Detection of fibre waviness using ultrasonic array scattering data. *J Nondestruct Eval*. 2013;32(3):215-227.
 26. Potter K, Khan B, Wisnom M, Bell T, Stevens J. Variability, fibre waviness and misalignment in the determination of the properties of composite materials and structures. *Compos A: Appl Sci Manuf*. 2008;39(9):1343-1354.
 27. Schmidt F, Rheinforth M, Horst P, Busse G. Effects of local fibre waviness on damage mechanisms and fatigue behaviour of biaxially loaded tube specimens. *Compos Sci Technol*. 2012;72(10):1075-1082.
 28. Shams S, Elhajjar R. Investigation into the effects of fiber waviness in standard notched composite specimens. *CEAS Aeronaut J*. 2015;6:1-15.
 29. Stecenko T, Piggott MR. Fiber waviness and other mesostructures in filament wound materials. *J Reinf Plast Compos*. 1997;16(18):1659-1674.
 30. Sutcliffe MPF, Lemanski SL, Scott AE. Measurement of fibre waviness in industrial composite components. *Compos Sci Technol*. 2012;72(16):2016-2023.
 31. Wang J, Potter KD, Hazra K, Wisnom MR. Experimental fabrication and characterization of out-of-plane fiber waviness in continuous fiber-reinforced composites. *J Compos Mater*. 2012;46(17):2041-2053.
 32. Wang J, Potter KD, Etches J. Experimental investigation and characterisation techniques of compressive fatigue failure of composites with fibre waviness at ply drops. *Compos Struct*. 2013;100:398-403.
 33. Wisnom MR. The effect of fibre waviness on the relationship between compressive and flexural strengths of unidirectional composites. *J Compos Mater*. 1994;28(1):66-76.
 34. Wisnom MR, Atkinson JW. Fibre waviness generation and measurement and its effect on compressive strength. *J Reinf Plast Compos*. 2000;19(2):96-110.
 35. Wooh SC, Daniel IM. Wave-propagation in composite-materials with fiber waviness. *Ultrasonics*. 1995;33(1):3-10.
 36. Noor AK, Shuart MJ, Starnes JH Jr, Willimas JG. Failure analysis and mechanisms of failure of fibrous composite structures. *NASA Conference Publication 2278*. Nasa Langley Research Center; 1982.
 37. Yang P, El-Hajjar R. Porosity defect morphology effects in carbon fiber—epoxy composites. *Polym-Plast Technol Eng*. 2012;15(11):1141-1148.
 38. Zhang A, Li D, Lu H, Zhang D. Qualitative separation of the effect of voids on the bending fatigue performance of hygrothermal conditioned carbon/epoxy composites. *Mater Des*. 2011;32:4803-4809.
 39. Kastner J, PB, Salaberger D, Sekelja J. Defect and porosity determination of fibre reinforced polymers by x-ray computed tomography. Proceedings of the 2nd International Symposium on NDT in Aerospace. 2010.
 40. De Andrade F, Silva JW, Muller BR, Hentschel MP, Portella PD, Chawla N. Three-dimensional microstructure visualization of porosity and Fe-rich inclusions in SiC particle-reinforced Al alloy matrix composites by X-ray synchrotron tomography. *Metall Mater Trans A*. 2010;41(8):2121-2128.
 41. Hardin RA, Beckermann C. Effect of porosity on the stiffness of cast steel. *Metall Mater Trans A*. 2007;38(12):2992-3006.

42. Lopes CS, Remmers J, Gurdal Z. *Influence of Porosity on the Interlaminar Shear Strength of Fibre-Metal Laminates*. American Institute of Aeronautics and Astronautics; 2006.
43. Hagstrand PO, Bonjour F, Manson JAE. The influence of void content on the structural flexural performance of unidirectional glass fibre reinforced polypropylene composites. *Compos A: Appl Sci Manuf*. 2005;36(5):705-714.
44. Costa ML, De Almeida SfM, Rezende MC. The influence of porosity on the interlaminar shear strength of carbon/epoxy and carbon/bismaleimide fabric laminates. *Compos Sci Technol*. 2001;61(14):2101-2108.
45. Daniel IM, Wooh SC, Komsky I. Quantitative porosity characterization of composite materials by means of Ultrasonic attenuation measurement. *J Nondestruct Eval*. 1992;11:1-8.
46. Daniel IM, Wooh SC, Komsky I. Quantitative porosity characterization of composite materials by means of ultrasonic attenuation measurements. *J Nondestruct Eval*. 1992;11(1):1-8.
47. Hsu DK, Uhl KM. A morphological study of porosity defects in graphite-epoxy composites. *Review of Progress in Quantitative Nondestructive Evaluation*. Springer; 1987:1175-1184.
48. Ma Y, Centea T, Nutt SR. Defect reduction strategies for the manufacture of contoured laminates using vacuum BAG-only prepregs. *Polym Compos*. 2015;38:2016-2025.

How to cite this article: El Hajjar RF, Pegoretti A, Movchan A, De Falco P, Pugno NM. The case study of a brittle failure of a mountain bike frame composed by carbon fiber reinforced plastic. *Polym Compos*. 2023;44(10):6349-6362. doi:[10.1002/pc.27563](https://doi.org/10.1002/pc.27563)